PAPER

# Performance and Stability Analysis for *ZJU* Glider


## AUTHORS

**Canjun Yang**
**Shilin Peng**
**Shuangshuang Fan**
The State Key Lab of Fluid Power Transmission and Control, Zhejiang University



## ABSTRACT

Underwater gliders provide an effective, low-cost method for sampling the ocean over large spatial and temporal scales. In this paper, we present a series of theoretical analyses to provide guidelines for vehicle design, which are used to develop a coastal 200-m-depth underwater glider known as the *Zhejiang University* (*ZJU*) glider. The *ZJU* glider uses a longitudinally actuated moving mass for pitch control and a rudder for turning control. Computational methods and analytical approaches are chosen to solve the viscous and inviscid terms of glider hydrodynamics, respectively. Steady flight equilibrium analysis gives the varied range of moving mass location for pitch control and varied vehicle volume for buoyancy control. Size analysis investigates the effects of glider geometric parameters on motion performance. For wings-level flight, we describe the variation in the maximum lift-to-drag ratio corresponding to a given vehicle size and speed. For turning motion, we investigate the manner in which the turning performance varies with vertical rudder configuration. Stability analysis determines the relationship between the stability of glider motion and the locations of the glider wings and rudder. Pool trials indicate that the *ZJU* glider functions well in water and is capable of serving as a sensor platform for ocean sampling.



Keywords: underwater glider, geometric parameters, hydrodynamic coefficients, design guidelines, pool trial


## Introduction

Underwater gliders are autonomous vehicles that move vertically by controlling buoyancy and horizontally by using wings. Since first envisioned by Stommel (1989), underwater gliders have received increasing attention worldwide and have become appealing sensor platforms for ocean observation (Rudnick et al., 2004). These vehicles provide an effective, low-cost method for sampling the ocean over large spatial and temporal scales. The first generation of underwater gliders has played a remarkable role in ocean sampling, including three legacy gliders: *Slocum* (Webb et al., 2001), *Seaglider* (Eriksen et al., 2001), and *Spray* (Sherman et al., 2001). Research and development on underwater gliders in China started at the beginning of this century (Wang & Wang, 2009), and several types of underwater gliders have been developed thus far. Shenyang Institute of Automation developed the *Sea-Wing* underwater glider with an operational depth of 1,200 m, which was designed for the application of deep-sea environment variable observation (Yu et al., 2011, 2013; Zhang et al., 2013). Tianjin University developed an experimental model of underwater glider propelled by environmental energy (Wang & Wang, 2009). The university also fabricated a hybrid-driven underwater glider named *Petrel*, which combines the features of legacy underwater gliders and conventional autonomous underwater vehicles (Wang et al., 2011). As the underwater glider is a technology undergoing active and rapid development, substantial theoretical analysis has been conducted on glider dynamics (Graver, 2005; Mahmoudian et al., 2010; Wang et al., 2011), performance, and stability (Jenkins et al., 2003; Yu et al., 2013) as well as motion control (Hussain et al., 2011; Leonard & Graver, 2001; Mahmoudian & Woolsey, 2008) and path planning (Mahmoudian, 2009; Mahmoudian et al., 2010). Glider geometry determines its hydrodynamic characteristics, having critical effects on glider dynamics, which in turn affects the performance and stability of glider motion. However, few systematic theoretical studies provide guidelines for glider development from this perspective.

This paper presents a series of theoretical analyses to provide guidelines for the design of a coastal 200-m-depth underwater glider, which is called *Zhejiang University* (*ZJU*) glider. These analytical methods can be applied to other glider designs as well. Because maneuverability is very important for a coastal glider, and a rudder has higher maneuverability

than a cylindrically actuated moving mass for turning motion, a rudder actuation scheme has been adopted for the *ZJU* glider. These analyses use the multibody dynamic model for a glider with a longitudinally actuated moving mass for pitch control and a rudder for turning control, which was derived by Fan et al. (2013). There are various approaches that can be used to determine the hydrodynamic coefficients of the glider for a given geometry. In our case, we adopt the computational method and analytical approach to obtain the viscous and inviscid coefficients, respectively. The theoretical analysis is conducted on the basis of the dynamic and hydrodynamic models.

Steady flight equilibrium analysis gives the varied range of moving mass for pitch control and the varied volume for buoyancy control, and size analysis investigates the effects of glider geometric parameters on motion performance. Because the lift-to-drag ratio can describe the efficiency of glider flight, for wings-level flight, we describe the variation in the maximum lift-to-drag ratio corresponding to a given vehicle size and speed. For turning motion, we investigate the manner in which the turning performance varies with the vertical rudder configuration. Stability analysis determines the relationship between the stability of the glider motion and the location of the glider wings and rudder by root locus investigation of glider longitudinal- and lateral-directional dynamics, respectively. On the basis of these systematic theoretical analyses, the *ZJU* glider is developed for serving as an ocean observatory platform operating in the East China Sea. Preliminary pool trials are carried out, which indicate that the *ZJU* glider functions well in water and is capable of serving as a sensor platform for ocean sampling.

## Geometry and Hydrodynamics

For any flight vehicle design, it is important to understand the relationship of vehicle geometry with performance and stability (Pamadi, 2004). Glider geometry determines the hydrodynamic characteristics, which further affect the performance and stability of vehicle motion. Glider geometric parameters are first defined in this section. We then introduce the calculation methods for the viscous and inviscid terms of *ZJU* glider hydrodynamics, respectively.

### Geometry and Nomenclature

Here, we consider a generic wing-and-cylinder configuration, where the cylindrical fuselage has diameter $d$ and length $l$. The wingspan (tip to tip) is $b$. We consider an untapered wing with a constant cross-sectional shape and a swept angle $\Lambda$. The wing platform area is denoted $S$. The mean aerodynamic chord length (i.e., the average width of a rectangular wing with equivalent aerodynamic properties) is $\bar{c}$ and $S = b \cdot \bar{c}$. An additional important geometric parameter is the maximum wing thickness $t$.

To simplify our parametric analysis, we describe the hull and wing geometry by using several nondimensional parameters including the hull fineness ratio ($f$), the wing aspect ratio ($AR$), the wingspan ratio ($\kappa$), and wing thickness ratio ($\bar{t}$).

$$f = \frac{l}{d}, AR = \frac{b^2}{S}, \kappa = \frac{b}{d}, \text{and } \bar{t} = \frac{t}{\bar{c}}.$$

We also consider several other configuration parameters for the wing and rudder, including wing longitudinal position $l_w$, vertical rudder longitudinal position $l_v$, and area of the rudder $S_v$. The aerodynamic center of the wing and the rudder, which is located near the quarter-chord line, are $\widetilde{l_w}$ and $\widetilde{l_v}$ (normalized by the fuselage length $l$) aft of the center of buoyancy, respectively, whereas the area of the rudder $S_v$ is normalized by the fuselage frontal area $S_f$. For the swept wing, the equivalent rectangular wing is obtained to determine the position of the wing. All of the geometric parameters that we considered are indicated in Figure 1.

### Hydrodynamic Characteristics

The hydrodynamic parameters include inviscid terms and viscous terms. There are several methods that can be used to produce results for hydrodynamic parameters based on a given geometry, including analytical, experimental, computational, and semi-empirical approaches (Geisbert, 2007). The distinctions between those methods have been discussed by Geisbert (2007). Depending on our needs and considering the calculation methods available, we chose a computational method based on computational fluid dynamics (CFD) software to determine the viscous terms of the glider hydrodynamics, and we used analytical approach to obtain the inviscid terms.

#### *Viscous Coefficients*

Some CFD programs are currently available, each having its own advantages and disadvantages. For each of these programs, a user defines a geometry, generates a grid pattern over the geometry, and applies the particular algorithm developed for that CFD

## FIGURE 1

Geometric parameters of the underwater glider model.

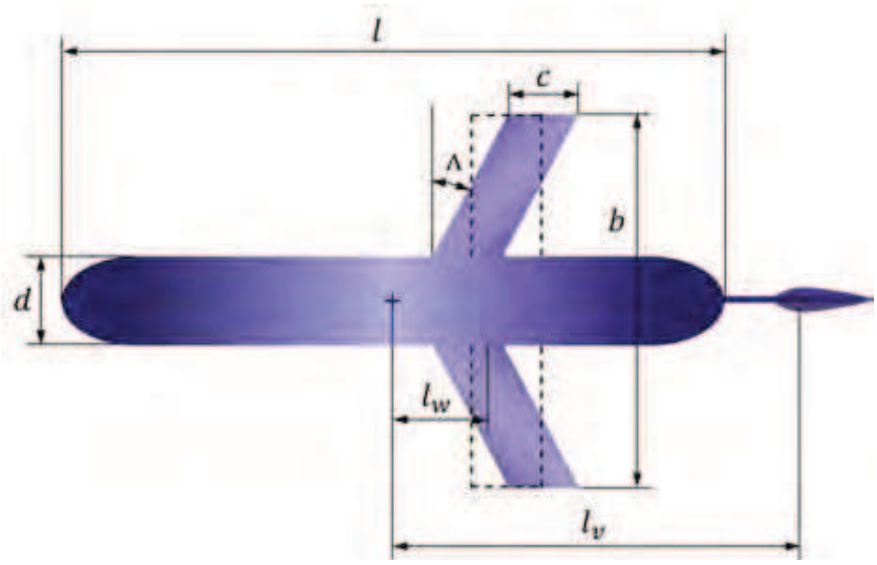


## TABLE 1

Geometry parameters of the *ZJU* glider.

| | |
|---|---|
| Fuselage full length *l* (m) | 1.940 |
| Fuselage diameter *D* (m) | 0.222 |
| Wing chord *c* (m) | 0.2 |
| Wing wingspan (m) | 0.536 |
| Rudder chord (m) | 0.2 |
| Rudder semi-wingspan (m) | 0.180 |
| Velocity | 0.400 m/s |

program (Geisbert, 2007); after data postprocessing, the viscid coefficients can be determined. In Zhang et al. (2013), the hydrodynamic coefficients of the *Sea-Wing* underwater glider are computed by using CFD software CFX, in which the simulation and data analysis procedures are based on dimensional hydrodynamic forces expressed in the current frame, and a ring-shaped fluid volume was assumed to rotate around the center of the ring to simulate the turning motion. Considering its familiarity, we used another CFD package FLUENT to solve for the viscous coefficients of the *ZJU* glider. In the simulation, the hydrodynamic forces were nondimensionalized and were expressed in the body frame. For glider roll, pitch, and yaw, a rotating reference frame was used to simulate these rotational motions by activating the moving reference frame model in FLUENT. Therefore, the simulation required only resetting the rotational velocity and the rotation axis origin when the rotational speed changed, without the need to regrid the fluid domain, which saved time and effort. The detailed solving methods are presented as follows:

(1) Computation model

Figure 2 gives the geometry of the *ZJU* glider in the design phase. Table 1 shows the geometry parameters, which are the fundamental data used to determine the hydrodynamic coefficients.

(2) Grid mesh method

The computational domain and mesh are shown in Figure 3. The fluid domain is set as $4l \times 4l \times 6l$, where $l$ is the full length of glider fuselage. To reduce the number of grids, we adopted the technique of local grid refinement for the key parts of the model, such as the wing and rudder, in which a C-O-type structured grid was constructed within the entire computational domain. In addition, we used an algebraic multigrid to accelerate the convergence of computation.

(3) Computational methodology

*Governing equations:*

The present simulation is based on solving Navier-Stokes equations by using the computational program. A second-order upwind solver was adopted along with the SIMPLE algorithm for pressure-velocity coupling. The governing equations

## FIGURE 2

*ZJU* glider geometry.

**FIGURE 3**

Computational domain and mesh distribution.

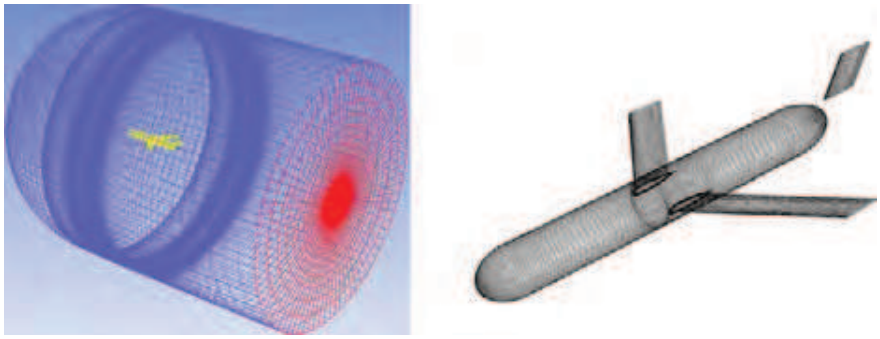

for viscous incompressible flow include the continuity equation and the momentum conservation equation, which are given by

$$\frac{\partial u_i}{\partial x_i} = 0 \tag{1}$$

$$\frac{\partial u_i}{\partial t} + \frac{\partial}{\partial x_j}\left(u_i u_j\right) = -\frac{1}{\rho}\frac{\partial p}{\partial x_i} + \nu\frac{\partial}{\partial x_j}\left[\frac{\partial u_i}{\partial x_j} + \frac{\partial u_j}{\partial x_i}\right] \tag{2}$$

where $u_i$ ($i$ = 1, 2, 3) are the velocity components in the direction of three coordinate axes, $x_i$ ($i$ = 1, 2, 3) are the coordinate components in the direction of three coordinate axes, $p$ is the pressure, $\rho$ is the density of fluid, $\nu$ is the kinematic viscosity, and $t$ is the time.

*Turbulence model:*

Because the governing equations are not closed, it is necessary to establish a turbulence model to make the governing equations solvable. Our calculation experiences indicate that the RNG $k-\varepsilon$ and SST $k-\omega$ are the most accurate models for solving the force derivatives and moment derivative, respectively.

*Boundary condition:*

The velocity of gliding is taken as the incoming flow for the inlet boundary condition, in which we have $v_{\text{in}} = v$. The pressure outlet was adopted for the outlet boundary.

(4) Data postprocessing

After numerical calculation, the computed forces and moments of fluid acting on the glider can be expressed in the body-fixed frame. By linear derivative regression, we can obtain the nondimensional coefficients of those forces and moments. The following expressions with nondimensional quantities provide definitions of viscous effects. These definitions largely follow the notational convention for aircraft (Nelson, 1989; Pamadi, 2004). We choose $0.5\rho V^2 l^2$ and $0.5\rho V^2 l^3$ as the dimensionless factors to nondimensionalize the viscous forces and moments as

$$X' = \frac{X}{0.5\rho V^2 l^2} \quad Y' = \frac{Y}{0.5\rho V^2 l^2} \quad Z' = \frac{Z}{0.5\rho V^2 l^2}$$
$$K' = \frac{K}{0.5\rho V^2 l^3} \quad M' = \frac{M}{0.5\rho V^2 l^3} \quad N' = \frac{N}{0.5\rho V^2 l^3}$$

$$X' = C_X(\alpha) = C_X^0 + C_X^\alpha \alpha^2 \qquad K' = C_K(\beta, \overline{p}, \delta_r) = C_K^\beta \beta + C_K^{\overline{p}} \overline{p} + C_K^\delta \delta_r$$
$$Y' = C_Y(\beta, \delta_r) = C_Y^\beta \beta + C_Y^\delta \delta_r \qquad M' = C_M(\alpha, \overline{q}) = C_M^\alpha \alpha + C_M^{\overline{q}} \overline{q}$$
$$Z' = C_Z(\alpha) = C_Z^\alpha \alpha \qquad N' = C_N(\beta, \overline{r}, \delta_r) = C_N^\beta \beta + C_N^{\overline{r}} \overline{r} + C_N^\delta \delta_r$$

where $\overline{p}, \overline{q}, \overline{r}$ are dimensionless angular velocity of glider, which is defined as $\overline{p} = \frac{pl}{V}, \overline{q} = \frac{ql}{V}, \overline{r} = \frac{rl}{V}$. The computed viscous coefficients of the *ZJU* glider are listed in Table 2.

Actually, the hydrodynamic forces and moments are generated in the "current" reference frame, and it is convenient to have an insight into glider flight characteristics by expressing hydrodynamic forces in this reference frame. Let $\alpha = \arctan(w / u)$ denote the vehicle's "angle of attack," and let $\beta = \arcsin(v/||\boldsymbol{v}||)$ denote the "sideslip angle." The current frame is related to the body frame through the proper rotation matrix (Etkin & Reid, 1996)

$$\boldsymbol{R}_{BC}(\alpha, \beta) = e^{-\widehat{\boldsymbol{e}}_2 \alpha} e^{\widehat{\boldsymbol{e}}_3 \beta}.$$

Then, we can write

$$\begin{pmatrix} D \\ SF \\ L \end{pmatrix} = \frac{1}{2}\rho V^2 l^2 \begin{pmatrix} C_D(\alpha) \\ C_{SF}(\beta, \delta_r) \\ C_L(\alpha) \end{pmatrix} = \boldsymbol{R}_{BC} \begin{pmatrix} X \\ Y \\ Z \end{pmatrix}$$

where $D$, $SF$, and $L$ are the drag, sideslip, and lift forces in the current frame, respectively. Referring to Graver (2005) and Bhatta (2006), the corresponding hydrodynamic coefficients can be expressed as

$$C_D(\alpha) = C_D^0 + K_d C_L(\alpha)^2, \quad C_{SF}(\beta, \delta_r) = C_{SF}^{\beta}\beta + C_{SF}^{\delta}\delta_r, \quad C_L(\alpha) = C_L^{\alpha}\alpha.$$

The coefficients in these expressions are also listed in Table 2.

### *Inviscid Coefficients*

In terms of the inviscid hydrodynamic coefficients, they are the components of the generalized added inertia matrix. According to SNAME notation (Fossen, 1995), the generalized added inertia matrix is

$$\mathbb{M}_{\mathrm{f}} = \begin{pmatrix} \boldsymbol{M}_f & \boldsymbol{C}_f^T \\ \boldsymbol{C}_f & \boldsymbol{J}_f \end{pmatrix} = -\begin{pmatrix} X_{\dot{u}} & X_{\dot{v}} & X_{\dot{w}} & X_{\dot{p}} & X_{\dot{q}} & X_{\dot{r}} \\ Y_{\dot{u}} & Y_{\dot{v}} & Y_{\dot{w}} & Y_{\dot{p}} & Y_{\dot{q}} & Y_{\dot{r}} \\ Z_{\dot{u}} & Z_{\dot{v}} & Z_{\dot{w}} & Z_{\dot{p}} & Z_{\dot{q}} & Z_{\dot{r}} \\ K_{\dot{u}} & K_{\dot{v}} & K_{\dot{w}} & K_{\dot{p}} & K_{\dot{q}} & K_{\dot{r}} \\ M_{\dot{u}} & M_{\dot{v}} & M_{\dot{w}} & M_{\dot{p}} & M_{\dot{q}} & M_{\dot{r}} \\ N_{\dot{u}} & N_{\dot{v}} & N_{\dot{w}} & N_{\dot{p}} & N_{\dot{q}} & N_{\dot{r}} \end{pmatrix}$$

where the component submatrices $\boldsymbol{M}_{\mathrm{f}}$, $\boldsymbol{J}_{\mathrm{f}}$, and $\boldsymbol{C}_{\mathrm{f}}$ represent added mass, added inertia and hydrodynamic coupling between the translational and rotational motion of the rigid body, respectively (Fossen, 1995). Due to the symmetry of the glider and considering the mainly effective terms, the generalized added inertia matrix turns out to be

$$\mathbb{M}_{\mathrm{f}} = \begin{pmatrix} \boldsymbol{M}_f & \boldsymbol{C}_f^T \\ \boldsymbol{C}_f & \boldsymbol{J}_f \end{pmatrix} = -\begin{pmatrix} X_{\dot{u}} & 0 & 0 & 0 & 0 & 0 \\ 0 & Y_{\dot{v}} & 0 & 0 & 0 & Y_{\dot{r}} \\ 0 & 0 & Z_{\dot{w}} & 0 & Z_{\dot{q}} & 0 \\ 0 & 0 & 0 & K_{\dot{p}} & 0 & 0 \\ 0 & 0 & M_{\dot{w}} & 0 & M_{\dot{q}} & 0 \\ 0 & N_{\dot{v}} & 0 & 0 & 0 & N_{\dot{r}} \end{pmatrix}$$

where $Y_{\dot{r}} = N_{\dot{v}}$ and $Z_{\dot{q}} = M_{\dot{w}}$ describe the asymmetric effects of the vertical rudder.

**TABLE 2**

Viscous coefficients of the *ZJU* glider.

| Notation | Value ($\times 10^{-3}$) |
|---|---|
| $C_X^0$ | –4.46 |
| $C_X^\alpha$ | 201.64 |
| $C_Y^\beta$ | –22.40 |
| $C_Y^\delta$ | –0.26 |
| $C_Z^\alpha$ | –254.53 |
| $C_K^\beta$ | –1.28 |
| $C_K^p$ | –5.99 |
| $C_K^\delta$ | –0.02 |
| $C_M^\alpha$ | –5.49 |
| $C_M^q$ | –4.92 |
| $C_N^\beta$ | –6.74 |
| $C_N^r$ | –7.69 |
| $C_N^\delta$ | 0.12 |
| $C_L^\alpha$ | –253.17 |
| $C_D^0$ | –4.44 |
| $K_d$ | 0.84 |

**TABLE 3**

Inviscid coefficients of the *ZJU* glider.

| Notation | Value |
|---|---|
| $X_{\dot{u}}$ | –1.502 |
| $Y_{\dot{v}}$ | –50.555 |
| $Z_{\dot{w}}$ | –74.702 |
| $K_{\dot{p}}$ | –4.415 |
| $M_{\dot{q}}$ | –9.637 |
| $N_{\dot{r}}$ | –11.748 |
| $Y_{\dot{r}}$ | 3.300 |
| $Z_{\dot{q}}$ | –6.433 |
| $M_{\dot{w}}$ | –6.433 |
| $N_{\dot{v}}$ | 3.300 |

The inviscid coefficients of the *ZJU* glider are determined by potential flow theory (Lewandowski, 2004). Analytical solutions are available for ellipsoids (in terms of elliptic integrals) and for a variety of simple two-dimensional shapes; two approximate methods are widely used to obtain values for the ellipsoid hull: the method of the "equivalent ellipsoid" and "strip theory." The contribution of appendages is generally computed separately and added to the hull contribution. In our case, the hull of glider is approximately regarded as a spheroid, and the appendages are approximately taken as the flat plates. Omitting the details of the calculation, the inviscid coefficients of the *ZJU* glider are shown in Table 3.

## Performance and Stability

This section present a series of theoretical analyses based on glider dynamic and hydrodynamic models to provide guidelines for glider design.

### Steady Flight Equilibrium Analysis

The purpose of this analysis is to obtain the basic parameters for glider design, which are the varied range of moving mass location $(\overline{r}_{p_x})$ for pitch control and the range of the volume of the ballast system $(\overline{V}_b)$. A numerical trim solver based on Matlab's *fsolve* subroutine was developed to calculate the steady flight equilibrium. Based on the desired steady motion parameters (speed, pitch angle, or heading angle), the numerical trim solver determines the required inputs for actuation, including the moving mass and rudder location, and the varied volume of the ballast system. The hydrodynamic coefficients used in the solver were obtained in Hydrodynamic Characteristics.

In our case, the moving mass for pitch control ($m_p$) is 8 kg, which was initially set at 0.45 m fore of the center of vehicle buoyancy; the mass of the buoyancy control module ($m_b$) is 6 kg, which was initially set at 0.6 m aft of the center of vehicle buoyancy; and the mass of glider rigid body ($m_{rb}$) is 50 kg, in which the center of mass is located 0.025 m vertically under the center of vehicle buoyancy. Tables 4 and 5 give two sets of wings-level equilibriums during glider descent. As noted in Table 4, for the same gliding speed $V$ = 0.2 m/s, when the pitch angle $\theta$ changes from –5° to –45°, the location of the moving mass $r_{p_x}$ varies from 466.4 to 606.9 mm, and the amount of volume variation $\tilde{V}_b$ varies from –208.4 to –48.7 ml. As shown in Table 5, for the same pitch angle $\theta$ = –35°, which is typically the maximum horizontal velocity flight condition of glider motion (Graver, 2005), when

**TABLE 4**

Wings-level equilibriums with fixed gliding velocity ($V$ = 0.2 m/s).

| $\theta$ (°) | $r_{p_x}$ (mm) | $\alpha$ (°) | $\tilde{V}_b$(ml) |
|---|---|---|---|
| –5 | 466.4 | 5.89 | –208.4 |
| –10 | 479.5 | 4.22 | –151.4 |
| –15 | 493.4 | 3.17 | –116.0 |
| –20 | 508.1 | 2.48 | –93.3 |
| –25 | 523.9 | 2.00 | –78.0 |
| -30 | 541.1 | 1.64 | –67.2 |
| –35 | 560.2 | 1.38 | –59.2 |
| –40 | 581.8 | 1.15 | –53.3 |
| –45 | 606.9 | 0.97 | –48.7 |
| –50 | 636.8 | 0.82 | –45.1 |

**TABLE 5**

Wings-level equilibriums with fixed pitch angle ($\theta$ = –35°).

| $V$ (m/s) | $r_{p_x}$(mm) | $\alpha$ (°) | $\tilde{V}_b$(ml) |
|---|---|---|---|
| 0.05 | 559.5 | 1.38 | –3.7 |
| 0.1 | 559.6 | 1.38 | –14.8 |
| 0.15 | 559.9 | 1.38 | –33.3 |
| 0.2 | 560.2 | 1.38 | –59.2 |
| 0.25 | 560.6 | 1.38 | –92.5 |
| 0.3 | 561.2 | 1.38 | –133.3 |
| 0.35 | 561.8 | 1.38 | –181.4 |
| 0.4 | 562.6 | 1.38 | –236.9 |

the gliding speed $V$ changes from 0.05 to 0.4 m/s, the required amount of volume variation $\tilde{V}_b$ varies from –3.7 to –236.9 ml, whereas the location of the moving mass $r_{p_x}$ does not change significantly, from 559.5 to 562.6 mm. Because wings-level equilibriums are symmetrical for glider descent and ascent motions, on the basis of numerical calculation of wings-level descent equilibrium, we chose $\overline{r}_{p_x}$ = ±200 mm and $\overline{V}_b$ = ±250 ml as our design parameters for glider development; thus, the maximum pitch angle of 50° and the maximum gliding speed of 0.4 m/s can be achieved.

## Size Analysis

A vehicle's geometry determines its performance, which further affects the performance of the vehicle. The size analysis takes both the wings-level flight and turning motion into consideration. Because the lift-to-drag ratio can describe the efficiency of glider flight, for wings-level flight, the effect of various geometric parameters on the speed at a minimum glide angle (also called the "speed to fly") and the maximum lift-to-drag ratio are considered. We focused on a few key parameters such as hull length, fineness ratio, wing aspect ratio, and wingspan ratio. For turning motion, we investigated the manner in which the turning performance varies with the vertical rudder configuration, such as the location and size of the rudder.

### *Wings-Level Flight*

Referring to Fan and Woolsey (2013), for flight at the shallowest descent angle, the parameters $C_D$, $C_L$, and $Re_l$ are

$$C_{D_{\mathrm{md}}} = 2C_{D_0},$$

$$C_{L_{\mathrm{md}}} = \sqrt{\frac{C_{D_0}}{K_d}} \text{ and } Re_{l_{\mathrm{md}}} = \frac{V_{\mathrm{md}} l}{\nu}.$$

At this flight condition, the maximum lift-to-drag ratio can be given by

$$\frac{L}{D} = \frac{C_{L_{\mathrm{md}}}}{C_{D_{\mathrm{md}}}} = \sqrt{\frac{1}{4K_d C_{D_0}}} \tag{3}$$

As $C_{D0}$ depends on the Reynolds number (Hoerner, 1965; Stengel, 2004), it varies with speed and length. On the basis of equation (3), we present a series of surface plots of the variation in the maximum lift-to-drag ratio based on the following *ZJU* glider parameter values:

$$l = 1.6\,\mathrm{m},\ m = 64\,\mathrm{kg},\ AR = 6.5,$$

$$\kappa = 6,\ f = 7,\ \text{and}\ \tilde{t} = 0.12.$$

Figure 4 gives variations in the maximum lift-to-drag ratio of a 64-kg glider, which is a function of minimum glide angle speeds and one of the four geometric parameters $l$, $AR$, $\kappa$, or $f$, whereas the nonvarying parameters take the nominal values given previously. The apparent discontinuities in the plot are due to the transition between laminar and turbulent flow.

## FIGURE 4

Variations of maximum lift-to-drag ratio with given minimum glide angle speeds and sizes. (a) Variation of maximum lift-to-drag ratio with $V_{md}$ and $l$. (b) Variation of maximum lift-to-drag ratio with $V_{md}$ and $AR$. (c) Variation of maximum lift-to-drag ratio with $V_{md}$ and $\kappa$. (d) Variation of maximum lift-to-drag ratio with $V_{md}$ and $f$.

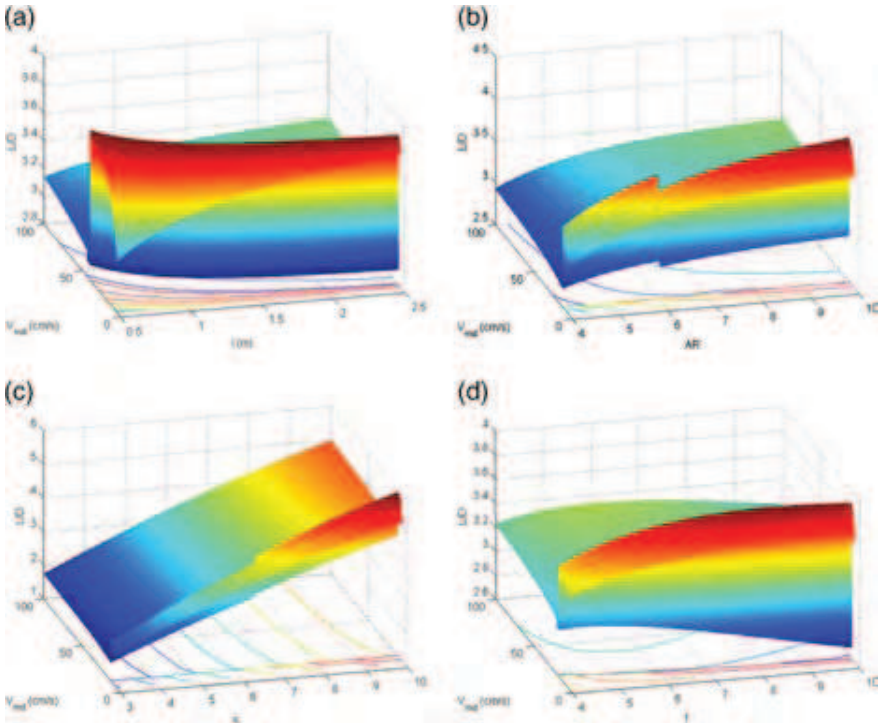


As can be seen in the figure, to increase the lift-to-drag ratio for a given minimum glide angle speed within a given flow regime (laminar or turbulent), the hull length $l$, wing aspect ratio $AR$, wingspan ratio $\kappa$, and hull fineness ratio $f$ should be increased. However, it is better to decrease the hull fineness ratio $f$ to obtain a higher lift-to-drag ratio when $V_{md}$ is more than 0.2 m/s.

### *Turning Motion*

In this section, we investigate the relationship between the turning performance and the vertical rudder configuration to provide guidelines for our vehicle design. Through simulation based on given vehicle dynamic models with chosen parameter values, numerical results of turning motions can be investigated. However, this numerical method could not present general conclusions about the relationship between parameter values and turning motion characteristics (Mahmoudian et al., 2010). In order to solve this problem, Mahmoudian et al. presented an approximate analytical expression for steady turning motion, which was derived by applying regular perturbation theory to a vehicle dynamic model. The analysis assumed that the glider turning was controlled by a lateral moving mass actuator. Because the *ZJU* glider is designed to turn by a rudder, we rederived the steady turning flight approximation by using the same method. In the process, a nominal, wings-level equilibrium flight condition was given at speed $V_0$ and pitch angle $\theta_0$, at some corresponding angle of attack $\alpha_0$, and the rudder deflection angle $\delta_r$ was set to zero so that the roll angle $\varphi$ and the sideslip angle $\beta$ were both zero. Then, we held the pitch angle $\theta_0$ unchanged and exerted a perturbation on the steady wings-level flight so that the body angular velocity vector $\boldsymbol{\omega}$ was vertical with a small magnitude $\varepsilon\omega_n$, where $\omega_n=\sqrt{g/l}$ is defined as the characteristic frequency and $\varepsilon$ denotes the perturbation parameter. When $\varepsilon = 0$, the glider performed steady gliding in the vertical plane; when $\varepsilon \neq 0$, the relationship between the glider parameters and $\varepsilon$ can be described as

$$V = \sum_n V_n \varepsilon^n = V_0 + \varepsilon V_1 + \varepsilon^2 V_2 + \cdots \qquad \eta = \sum_n \eta_n \varepsilon^n = \eta_0 + \varepsilon \eta_1 + \varepsilon^2 \eta_2 + \cdots$$
$$\alpha = \sum_n \alpha_n \varepsilon^n = \alpha_0 + \varepsilon \alpha_1 + \varepsilon^2 \alpha_2 + \cdots \qquad \phi = \sum_n \phi_n \varepsilon^n = \varepsilon \phi_1 + \varepsilon^2 \phi_2 + \cdots$$
$$\beta = \sum_n \beta_n \varepsilon^n = \varepsilon \beta_1 + \varepsilon^2 \beta_2 + \cdots \qquad \delta_r = \sum_n \delta_m \varepsilon^n = \varepsilon \delta_{r1} + \varepsilon^2 \delta_{r2} + \cdots$$

To obtain the parameter of steady turning motion, we substituted these equations into the dynamic equations and set the dynamic equations to zero. After some algebraic operations, we can find that

$$
\begin{aligned}
&V \approx V_0, \quad \varphi \approx \varepsilon\varphi_1,\\
&\alpha \approx \alpha_0, \quad \beta \approx \varepsilon\beta_1,\\
&\eta \approx \eta_0, \quad \delta_{\mathrm{r}} \approx \varepsilon\delta_{\mathrm{r1}},
\end{aligned}
$$

where $\varphi_1$, $\beta_1$, and $\delta_{r1}$ are explicitly given as

$$
\begin{aligned}
\delta_{\mathrm{r1}} = {} & (\omega_n((l^2(C_N^\beta l\mathrm{V}_{NB}\eta_0 - C_Y^\beta m_{\mathrm{b}} r_{\mathrm{b}_0} - C_Y^\beta m_{\mathrm{p}} r_{p_0})\rho + 2\mathrm{V}_{NB}\eta_0(X_{\dot{u}} - Y_{\dot{v}})\cos\alpha_0)(2C_Y^\beta l^2(M_{\dot{w}} + N_{\dot{v}})\rho\cos\theta_0\sin\alpha_0\\
& + 2\cos\alpha_0\cos\theta_0(l^2(C_Y^\beta m_{\mathrm{rb}} r_{\mathrm{rb}_0} + C_K^\beta l(m + X_{\dot{u}}))\rho + 2(m + X_{\dot{u}})(Y_{\dot{v}} - Z_{\dot{w}})\sin\alpha_0)\\
& + (-C_K^p C_Y^\beta l^6\rho^2 + 2l^2(C_Y^\beta m_{\mathrm{rb}} r_{\mathrm{rb}_0} + C_K^\beta l(m + Z_{\dot{w}}))\rho\sin\alpha_0 + 4(Y_{\dot{v}} - Z_{\dot{w}})(m + Z_{\dot{w}})(\sin\alpha_0)^2\sin\theta_0)\\
& - (l^2(C_K^\beta l\mathrm{V}_{NB}\eta_0 + C_Y^\beta m_{\mathrm{rb}} r_{\mathrm{rb}_0})\rho + 2\mathrm{V}_{NB}\eta_0(Y_{\dot{v}} - Z_{\dot{w}})\sin\alpha_0)(C_Y^\beta l^2\rho((C_N^r l^4\rho - 2(N_{\dot{v}} + m_{\mathrm{b}} r_{\mathrm{b}_0} + m_{\mathrm{p}} r_{p_0})\cos\alpha_0)\cos\theta_0\\
& + 2\left(M_{\dot{w}} - m_{\mathrm{b}} r_{\mathrm{b}_0} - m_{\mathrm{p}} r_{p_0}\right)\sin\alpha_0\sin\theta_0) + 2(C_N^\beta l^3\rho + 2(X_{\dot{u}} - Y_{\dot{v}})\cos\alpha_0)((m + X_{\dot{u}})\cos\alpha_0\cos\theta_0\\
& + (m + Z_{\dot{w}})\sin\alpha_0\sin\theta_0))))/(-C_Y^\beta l^4 V_0\rho^2(l^3(C_K^\delta(C_N^\beta l\mathrm{V}_{NB}\eta_0 - C_Y^\beta m_{\mathrm{b}} r_{\mathrm{b}_0} - C_Y^\beta m_{\mathrm{p}} r_{p_0})\\
& - C_K^\beta\left(C_N^\delta l\mathrm{V}_{NB}\eta_0 - C_Y^\delta m_{\mathrm{b}} r_{\mathrm{b}_0} - C_Y^\delta m_{\mathrm{p}} r_{p_0}\right) + (-C_N^\delta C_Y^\beta + C_N^\beta C_Y^\delta)m_{\mathrm{rb}} r_{\mathrm{rb}_0})\rho + 2(C_K^\delta l\mathrm{V}_{NB}\eta_0\\
& + C_Y^\delta m_{\mathrm{rb}} r_{\mathrm{rb}_0})(X_{\dot{u}} - Y_{\dot{v}})\cos\alpha_0 - 2(C_N^\delta l\mathrm{V}_{NB}\eta_0 - C_Y^\delta m_{\mathrm{b}} r_{\mathrm{b}_0} - C_Y^\delta m_{\mathrm{p}} r_{p_0})(Y_{\dot{v}} - Z_{\dot{w}})\sin\alpha_0));
\end{aligned}
\tag{4}
$$

$$
\begin{aligned}
\varphi_1 = {} & (V_0\omega_n(4(-C_Y^\delta m_{\mathrm{rb}} r_{\mathrm{rb}_0} + C_K^\delta l(m + X_{\dot{u}})(X_{\dot{u}} - Y_{\dot{v}})(\cos\alpha_0)^2 + 2l^3\rho\sec\theta_0\sin\alpha_0((C_N^\delta C_Y^\beta(M_{\dot{w}} + N_{\dot{v}})\\
& - C_Y^\delta(C_N^\beta(M_{\dot{w}} + N_{\dot{v}}) + C_N^r l(-Y_{\dot{v}} + Z_{\dot{w}})))\cos\theta_0 + ((C_N^\delta C_Y^\beta - C_N^\beta C_Y^\delta)m_{\mathrm{rb}} r_{\mathrm{rb}_0} + C_K^\delta(C_Y^\beta(-M_{\dot{w}} + m_{\mathrm{b}} r_{\mathrm{b}_0} + m_{\mathrm{p}} r_{p_0})\\
& + C_N^\beta l(m + Z_{\dot{w}})) - C_K^\beta(C_Y^\delta(-M_{\dot{w}} + m_{\mathrm{b}} r_{\mathrm{b}_0} + m_{\mathrm{p}} r_{p_0}) + C_N^\delta l(m + Z_{\dot{w}})))\sin\theta_0 - 4(Y_{\dot{v}} - Z_{\dot{w}})(C_Y^\delta(-M_{\dot{w}} + m_{\mathrm{b}} r_{\mathrm{b}_0} + m_{\mathrm{p}} r_{p_0})\\
& + C_N^\delta l(m + Z_{\dot{w}}))(\sin\alpha_0)^2\tan\theta_0 + l^7\rho^2(-C_K^\delta C_N^r C_Y^\beta + C_K^\beta C_N^r C_Y^\delta + C_K^p(-C_N^\delta C_Y^\beta + C_N^\beta C_Y^\delta)\tan\theta_0)\\
& + 2\cos\alpha_0(l^3((C_N^\delta C_Y^\beta - C_N^\beta C_Y^\delta)m_{\mathrm{rb}} r_{\mathrm{rb}_0} + C_K^\delta(C_Y^\beta(N_{\dot{v}} + m_{\mathrm{b}} r_{\mathrm{b}_0} + m_{\mathrm{p}} r_{p_0}) + C_N^\beta l(m + X_{\dot{u}})\\
& - C_K^\beta(C_Y^\delta\left(N_{\dot{v}} + m_{\mathrm{b}} r_{\mathrm{b}_0} + m_{\mathrm{p}} r_{p_0}\right) + C_N^\delta l(m + X_{\dot{u}})))\rho - 2(C_Y^\delta(M_{\dot{w}}(X_{\dot{u}} - Y_{\dot{v}}) + N_{\dot{v}}(X_{\dot{u}} - Z_{\dot{w}})\\
& + \left(m_{\mathrm{b}} r_{\mathrm{b}_0} + m_{\mathrm{p}} r_{p_0}\right)(Y_{\dot{v}} - Z_{\dot{w}})) + C_N^\delta l(m + X_{\dot{u}})(Y_{\dot{v}} - Z_{\dot{w}}))\sin\alpha_0 + (X_{\dot{u}} - Y_{\dot{v}})(C_K^p C_Y^\delta l^4\rho\\
& + 2(-C_Y^\delta m_{\mathrm{rb}} r_{\mathrm{rb}_0} + C_K^\delta l(m + Z_{\dot{w}})\sin\alpha_0\tan\theta_0))))/(2g(l^3(C_K^\delta(C_N^\beta l\mathrm{V}_{NB}\eta_0 + C_Y^\beta m_{\mathrm{b}} r_{\mathrm{b}_0} + C_Y^\beta m_{\mathrm{p}} r_{p_0})\\
& - C_K^\beta\left(C_N^\delta l\mathrm{V}_{NB}\eta_0 + C_Y^\delta m_{\mathrm{b}} r_{\mathrm{b}_0} + C_Y^\delta m_{\mathrm{p}} r_{p_0}\right) + (C_N^\delta C_Y^\beta - C_N^\beta C_Y^\delta)m_{\mathrm{rb}} r_{\mathrm{rb}_0})\rho + 2(C_K^\delta l\mathrm{V}_{NB}\eta_0 - C_Y^\delta m_{\mathrm{b}} r_{\mathrm{b}_0})(X_{\dot{u}} - Y_{\dot{v}})\cos\alpha_0\\
& - 2\left(C_N^\delta l\mathrm{V}_{NB}\eta_0 + C_Y^\delta m_{\mathrm{b}} r_{\mathrm{b}_0} + C_Y^\delta m_{\mathrm{p}} r_{p_0}\right)(Y_{\dot{v}} - Z_{\dot{w}})\sin\alpha_0));
\end{aligned}
\tag{5}
$$

$$
\begin{aligned}
\beta_1 = {} & -(\omega_n(\cos\theta_0(C_N^r l^4\left(C_K^\delta l\mathrm{V}_{NB}\eta_0 + C_Y^\delta m_{\mathrm{rb}} r_{\mathrm{rb}_0}\right)\rho + 2(C_K^\delta l(-\mathrm{V}_{NB}\eta_0(N_{\dot{v}} + m_{\mathrm{b}} r_{\mathrm{b}_0} + m_{\mathrm{p}} r_{p_0}) + (m_{\mathrm{b}} r_{\mathrm{b}_0} + m_{\mathrm{p}} r_{p_0})(m + X_{\dot{u}}))\\
& + m_{\mathrm{rb}} r_{\mathrm{rb}_0}(-C_Y^\delta N_{\dot{v}} + C_N^\delta l(m - \mathrm{V}_{NB}\eta_0 + X_{\dot{u}})))\cos\alpha_0 - 2(M_{\dot{w}} + N_{\dot{v}})(C_N^\delta l\mathrm{V}_{NB}\eta_0 - C_Y^\delta m_{\mathrm{b}} r_{\mathrm{b}_0} - C_Y^\delta m_{\mathrm{p}} r_{p_0})\sin\alpha_0)\\
& + (C_K^p l^4\left(C_N^\delta l\mathrm{V}_{NB}\eta_0 - C_Y^\delta m_{\mathrm{b}} r_{\mathrm{b}_0} - C_Y^\delta m_{\mathrm{p}} r_{p_0}\right)\rho + 2(C_K^\delta l(\mathrm{V}_{NB}\eta_0(M_{\dot{w}} - m_{\mathrm{b}} r_{\mathrm{b}_0} - m_{\mathrm{p}} r_{p_0}) + (m_{\mathrm{b}} r_{\mathrm{b}_0} + m_{\mathrm{p}} r_{p_0})(m + Z_{\dot{w}}))\\
& + m_{\mathrm{rb}} r_{\mathrm{rb}_0}(C_Y^\delta M_{\dot{w}} + C_N^\delta l(m - \mathrm{V}_{NB}\eta_0 + Z_{\dot{w}})))\sin\alpha_0)\sin\theta_0))/(V_0(l^3(C_K^\delta(C_N^\beta l\mathrm{V}_{NB}\eta_0 - C_Y^\beta m_{\mathrm{b}} r_{\mathrm{b}_0}\\
& - C_Y^\beta m_{\mathrm{p}} r_{p_0}) - C_K^\beta\left(C_N^\delta l\mathrm{V}_{NB}\eta_0 - C_Y^\delta m_{\mathrm{b}} r_{\mathrm{b}_0} - C_Y^\delta m_{\mathrm{p}} r_{p_0}\right) + (-C_N^\delta C_Y^\beta + C_N^\beta C_Y^\delta)m_{\mathrm{rb}} r_{\mathrm{rb}_0})\rho + 2(C_K^\delta l\mathrm{V}_{NB}\eta_0\\
& + C_Y^\delta m_{\mathrm{rb}} r_{\mathrm{rb}_0})(X_{\dot{u}} - Y_{\dot{v}})\cos\alpha_0 - 2(C_N^\delta l\mathrm{V}_{NB}\eta_0 - C_Y^\delta m_{\mathrm{b}} r_{\mathrm{b}_0} - C_Y^\delta m_{\mathrm{p}} r_{p_0})(Y_{\dot{v}} - Z_{\dot{w}})\sin\alpha_0)).
\end{aligned}
\tag{6}
$$

Because turning motions can be parameterized by the rudder deflection angle ($\delta_r$), the glider roll angle ($\varphi$), and the sideslip angle ($\beta$), equations (4), (5), and (6) give the approximate expressions of turning motion, on the basis of which, we can investigate the relationship between the turning capability and the vertical rudder configuration (rudder longitudinal position $l_v$ and the area of rudder $S_v$). Although the rudder configurations $l_v$ and $S_v$ do not appear explicitly in equations (4), (5), and (6), they do influence turning performance by affecting the hydrodynamic coefficients, such as $C_Y^\beta$, $C_Y^\delta$, $C_K^\beta$, $C_K^p$, $C_K^\delta$, $C_N^\beta$, $C_N^r$, $C_N^\delta$. Related explicit expressions have been reported by Nelson (1989).

To determine the manner in which the rudder configuration affects the turning capability, we examined the variations of the first-order sensitivities $\delta_{r1}$, $\varphi_1$, and $\beta_1$ with $l_v$ and $S_v$ for a given turn rate. The approximate values of $\delta_r$, $\varphi$, and $\beta$ can be calculated by multiplying the parameters $\delta_{r1}$, $\varphi_1$, and $\beta_1$ by the perturbation parameter $\varepsilon$, which is proportional to the

turning rate. Figure 5 shows the plots generated by equations (4), (5), and (6), in which the steady wings-level equilibrium is $V_0$ = 0.4 m/s, $\theta_0$ = 34.1°, and $\alpha_0$ = 1.4°. As can be seen in the figure, when $l_v$ or $S_v$ is small, a smaller rudder deflection angle is needed to finish a given steady turn rate, suggesting that a smaller $l_v$ or $S_v$ yields greater turning ability. We used a 0.01-rad/s turn rate for example, in which the corresponding variations of $\delta_r$, $\varphi$, and $\beta$ with $l_v$ and $S_v$ are presented in Figure 6. Considering the turning control authority as well as the stability discussed in Stability Analysis, we chose $S_v$ = 0.038 m$^2$ and $l_v$ = 1.072 m as the rudder configuration. The turning parameters of the *ZJU* glider with the chosen rudder configuration are marked by green crosses in Figure 6. The figure shows that the turning capability of the *ZJU* glider is acceptable with the chosen ruder configuration.

**FIGURE 5**

Variation in turning parameters $\delta_1$, $\varphi_1$, and $\beta_1$ with $l_v$ and $S_v$. (a) Variation of turning parameters with $l_v$. (b) Variation of turning parameters with $S_v$.

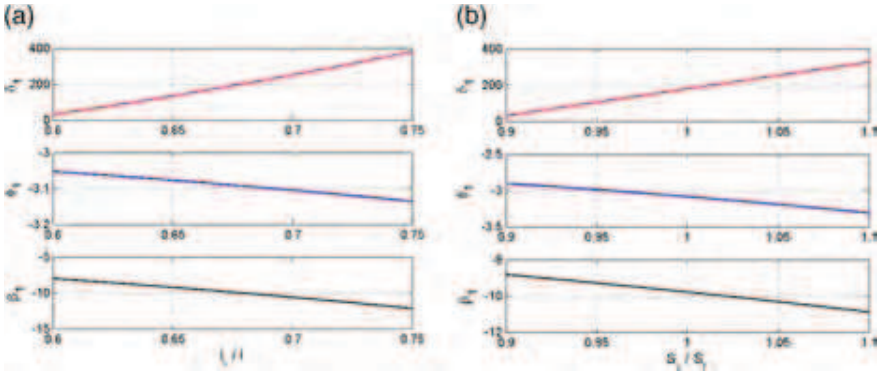


**FIGURE 6**

Variation in turning parameters $\delta$, $\varphi$, and $\beta$ with $l_v$ and $S_v$. (a) Variation of turning parameters with $l_v$. (b) Variation of turning parameters with $S_v$.

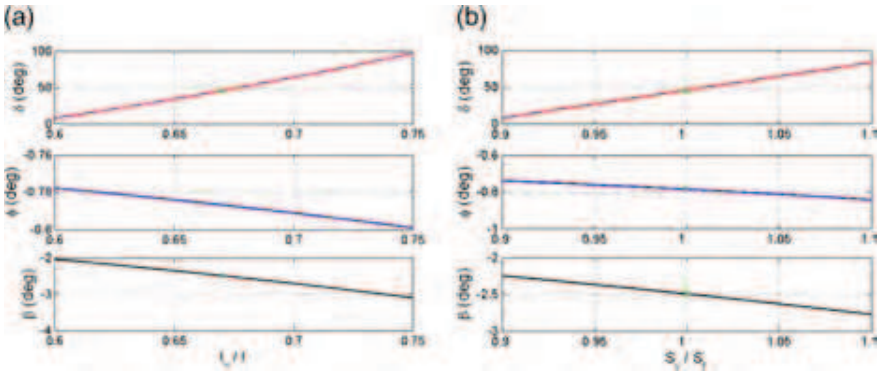


## Stability Analysis

A glider's geometry not only affects glider flight performance but also has an effect on the stability of glider motion. Fan and Woolsey (2013) examined the effects of glider geometry on motion stability by root locus analysis. In their study, however, glider turning motion was achieved by rolling. Considering a glider with a rudder for turning control, we adopted the same procedure to investigate the effects of glider design parameters on glider motion stability to determine these design parameters.

### *Eigenmode Analysis*

To investigate the natural modes and stability of the glider motion, we assumed that the glider operates under certain steady flight conditions, and then we linearized the dynamic equations about this equilibrium point. Specifically, the case of steady flight at maximum horizontal speed was considered. By using the same steady flight equilibrium analysis approach described in Steady Flight Equilibrium Analysis, we obtained the equilibrium:

$$V_{eq} = 0.4\ \text{m/s}, \tilde{W}_{eq} = 2.3804\ \text{N}, \theta_{eq} = -0.5957\text{rad}, r_{px\,eq} = 0.5041\ \text{m}, \alpha_{eq} = 0.0251\ \text{rad}.$$

We linearized the dynamic equations about the equilibrium point. The resulting equations can be decomposed into longitudinal and lateral-directional components (Nelson, 1989; Schmidt, 1998), each of which is a set of four first-order equations. Ignoring certain kinematic variables gives the equations:

$$\dot{\boldsymbol{X}}_{long} = \boldsymbol{A}_{long}\boldsymbol{X}_{long} + \boldsymbol{B}_{long}\boldsymbol{u}_{long} \quad \text{and} \quad \dot{\boldsymbol{X}}_{lat} = \boldsymbol{A}_{lat}\boldsymbol{X}_{lat} + \boldsymbol{B}_{lat}\boldsymbol{u}_{lat}$$

where

$$\boldsymbol{X}_{long} = [\Delta u, \Delta w, \Delta q, \Delta\theta]^T \quad \text{and} \quad \boldsymbol{X}_{lat} = [\Delta v, \Delta p, \Delta r, \Delta\varphi]^T$$

are the state matrices and $\boldsymbol{u}_{long}$ and $\boldsymbol{u}_{lat}$ are the input matrices. The elements of the state and input matrices depend on the steady flight condition and the glider geometry. Tables 6 and 7 give the eigenvalues $\lambda$ and nondimensional eigenvectors $\boldsymbol{v}$ (in amplitude and phase form) for the state matrices $\boldsymbol{A}_{long}$ and $\boldsymbol{A}_{lat}$.

As shown in Table 6, the eigenvalues of longitudinal motion include two real eigenvalues and a complex conjugate pair. Examination of the corresponding eigenvectors gives the following characteristic modes:

- A quickly converging angle of attack mode.
- A quickly converging forward speed mode.
- An underdamped mode involving the pitch rate and pitch angle.

Table 7 shows that the eigenvalues of lateral-directional motion also include two real eigenvalues and a complex conjugate pair. Examination of the corresponding eigenvectors gives the following characteristic modes:

- A quickly converging yaw rate mode.
- An underdamped mode in which the roll rate, yaw rate, and roll angle are strongly coupled.

### *Glider Stability Varied With Geometry*

Here, we examine the effects of some glider design parameters on glider stability by root locus analysis. These glider design parameters include longitudinal wing location $l_w$, vertical rudder longitudinal position $l_v$, and the area of vertical rudder $S_v$. Variation of parameters $l_w$, $l_v$, and $S_v$ changes the hydrodynamic coefficients and thus affects glider stability.

The physical and hydrodynamic characteristics used in this analysis are based on the data of the *ZJU* glider in the design phase. Two specific flight conditions are considered: flight at maximum horizontal speed and flight at minimum glide angle. Because the stability of steady motion is affected by vehicle speed, we fixed the flight speed at $V = 0.4$ m/s to reasonably compare different flight conditions.

For longitudinal modes, we preset root locus plots in terms of longitudinal wing location $l_w$. Figure 7(a) shows the root locus plots at the maximum speed flight condition, and Figure 7 (b) shows the plots at the minimum glide angle flight condition. In these plots, $l_w$ varies from zero (denoted by red circles, in which case, the wing is aligned with the center of buoyancy) to $0.25l$ (denoted by blue squares). It can be seen in the figure that the farther aft the wing is located, the more stable the glider longitudinal dynamics become. This result may be partly due to the increased pitch damping.

For the lateral-directional modes, we preset the root locus plots in terms of $l_v$ and $S_v$. Figure 8(a) shows the root locus plots in flight at maximum speed, and Figure 8(b) shows the plots in flight at the minimum glide angle. In these plots, $l_v$ varies from $0.5l$ to $l$ (from the stern of the hull to a half-vehicle length aft of the

**TABLE 6**

Eigenvalues and eigenvectors of longitudinal motion.

| **Longitudinal** | $\lambda_1 = -1.57$ | $\lambda_2 = -0.12$ | $\lambda_3 = -0.01 + i$ | $\lambda_4 = -0.01 - i$ |
|---|---|---|---|---|
| $\Delta u$ | $v_{11} = 0.08\angle 0°$ | $v_{21} = 1\angle 180°$ | $v_{31} = 0.02\angle 47.3°$ | $v_{41} = 0.02\angle -47.3°$ |
| $\Delta w$ | $v_{12} = 1\angle 180°$ | $v_{22} = 0.05\angle 0°$ | $v_{32} = 0.1\angle -43.5°$ | $v_{42} = 0.1\angle 43.5°$ |
| $\Delta q$ | $v_{13} = 0.45\angle 0°$ | $v_{23} = 0.003\angle 180°$ | $v_{33} = 1\angle 0°$ | $v_{43} = 1\angle 0°$ |
| $\Delta\theta$ | $v_{14} = 0.28\angle 180°$ | $v_{24} = 0.03\angle 0°$ | $v_{34} = 0.99\angle -90.7°$ | $v_{44} = 0.99\angle 90.7°$ |

**TABLE 7**

Eigenvalues and eigenvectors of lateral-directional motion.

| **Lateral** | $\lambda_1 = -0.32 + 0.94i$ | $\lambda_2 = -0.32 - 0.94i$ | $\lambda_3 = 0.25$ | $\lambda_4 = -0.59$ |
|---|---|---|---|---|
| $\Delta v$ | $v_{11} = 0.24\angle -100.1°$ | $v_{21} = 0.24\angle 100.1°$ | $v_{31} = 0.52\angle 0°$ | $v_{41} = 0.51\angle 0°$ |
| $\Delta p$ | $v_{12} = 0.87\angle 26.7°$ | $v_{22} = 0.87\angle -26.7°$ | $v_{32} = 0.06\angle 180°$ | $v_{42} = 0.13\angle 0°$ |
| $\Delta r$ | $v_{13} = 1\angle 180°$ | $v_{23} = 1\angle 180°$ | $v_{33} = 1\angle 180°$ | $v_{43} = 1\angle 0°$ |
| $\Delta\varphi$ | $v_{14} = 0.89\angle -82.2°$ | $v_{24} = 0.89\angle 82.2°$ | $v_{34} = 0.22\angle 180°$ | $v_{44} = 0.22\angle 180°$ |

## FIGURE 7

Root locus plots for longitudinal modes with the parameter $l_w$. Root locus branches begin at red circles and end at blue squares. The green crosses represent the eigenvalues of glider longitudinal dynamics with chosen design parameters. (a) Flight at maximum speed. (b) Flight at minimum glide angle.

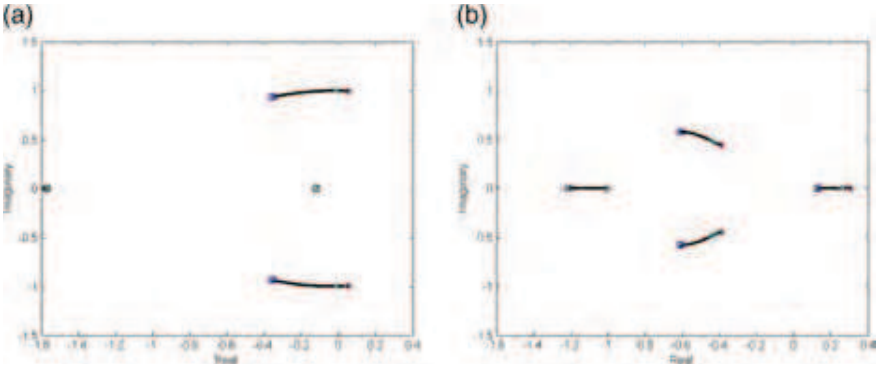


## FIGURE 8

Root loci for lateral-directional modes with parameter $l_v$. Root locus branches begin at red circles and end at blue squares. The green crosses represent the eigenvalues of glider lateral-directional dynamics with chosen design parameters. (a) Flight at maximum speed. (b) Flight at minimum glide angle.

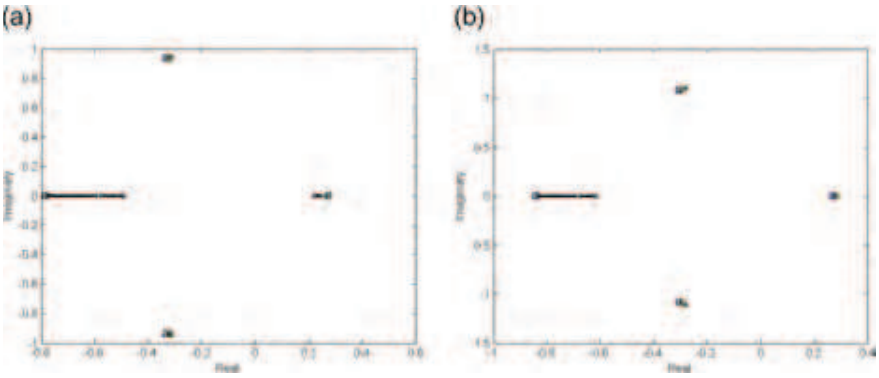


stern). It can be seen in the figure that the farther aft the vertical rudder is located, the more stable the glider lateral-directional dynamics become. This result may be due to increased yaw stiffness and damping. Figure 9(a) shows root locus plots at the maximum speed flight condition, and Figure 9(b) shows the plots at the minimum glide angle flight condition, all in terms of the parameter $S_v$. In these plots, $S_v$ varies from half of the hull frontal area to 1.5 times the hull frontal area. It can be seen in the figure that the larger the rudder area, the more stable the glider lateral-directional dynamics become because of increased yaw stiffness and damping.

From the aforementioned results, we have clarified how to determine the design parameters to enhance glider stability. However, greater stability implies that greater control authority is required to affect a maneuver such as a turn. Considering the turning motion analysis described in Turning Motion, the following design parameters were chosen for glider development: $l_w$ = 0.152 m, $S_v$ = 0.0.38 m$^2$, and $l_v$ = 1.072 m. The eigenvalues with the glider design parameters are also marked by green crosses in Figures 7, 8, and 9.

## Pool Trials

Theoretical analysis provides guidelines for the vehicle design; on the basis of which, we completed the development of the *ZJU* glider. After system trimming, the glider prototype was tested in a rectangular swimming pool of dimension 50 m × 16 m and with a maximum depth of 3.5 m. During the tests, the glider communicated with an onshore control computer

## FIGURE 9

Root loci for lateral-directional modes with parameter $S_v$. Root locus branches begin at red circles and end at blue squares. The green crosses represent the eigenvalues of glider lateral-directional dynamics with chosen design parameters. (a) Flight at maximum speed. (b) Flight at minimum glide angle.

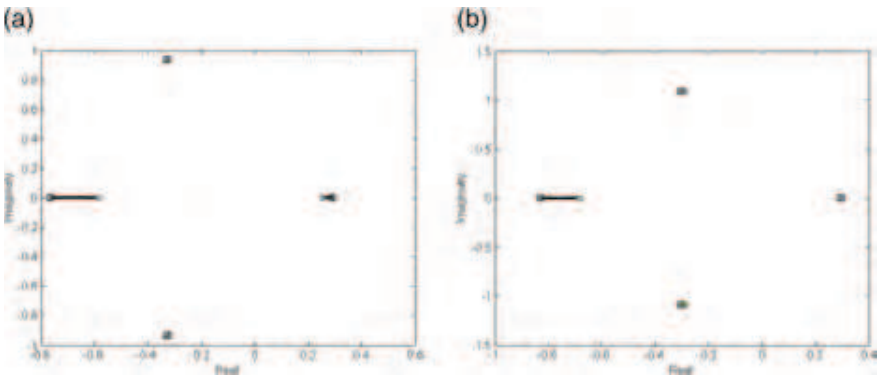

when it appeared on the surface of the water via radio, receiving instructions and sending data collected by onboard sensors. The pool trials aimed to validate the performance of the glider prototype, including the sawtooth motion test and the turning motion test. Moreover, a pitch control test was conducted to investigate the relationship between moving mass displacement and glider pitch angle, and a buoyancy control test was conducted to examine the relationship between the varied volume of the buoyancy system and the glide speed. These experimental results can be used as a reference for the future design of motion control algorithms.

### Sawtooth Motion Test

The main objective of the sawtooth motion test is to evaluate the cooperating ability of glider motion modules for attitude and buoyancy control. In this test, the rudder deflection angle was set to be zero such that the glider moved in the vertical plane. The glider followed an up-and-down, sawtooth profile through the water. Figure 10 shows the glider during its descent and ascent, which were captured by an underwater camera.

### Turning Motion Test

In the turning motion test, the rudder deflection angle was set to 60°. Figure 11 shows the turning motion during ascent, which was recorded by a camera. During the ascent, the glider turned roughly 32° in 40 s, resulting in a turn rate of approximately 0.014 rad/s. This turning test validated the turning module design of the glider.

### Pitch Control Test

The pitch control test was conducted to evaluate the performance of glider pitch control and to investigate the relationship between moving mass displacement and glider pitch angle. During the test, the volume of the buoyancy control system $\tilde{V}_b$ was fixed at −160 ml for descent or 160 ml for ascent, and the moving mass location for pitch control varied. A set of measurements was obtained, which is represented by the red square in Figure 12. These measurements were compared with the numerical results calculated by the numerical trim solver for steady flight equilibrium, as shown by the blue curve in Figure 12. We can find that the measured results agree with the calculated results, which validates the accuracy of the calculated results of the numerical trim solver and also indicates that the *ZJU* glider is capable of the expected performance of pitch control.

### Buoyancy Control Test

The buoyancy control test was conducted in order to understand the relationship between the varied volume of the buoyancy system and the glide speed. In the test, the moving mass displacement was fixed at 32 mm for descent or −32 mm for ascent. Because inertial velocity measurements are typically unavailable for an underwater glider, depth rate is generally used to describe the glide speed and is used for dead reckoning. In the buoyancy control test, the depth rate was calculated by the onshore control computer according to the sampling rate, and the depth was measured by an onboard pressure sensor. The measure data are represented by the red square in Figure 13. The figure also includes the numerical results of the steady flight calculated by the numerical trim solver, which are shown by the blue curve. It can be seen that the experimental results agree with the calculated results, which validates the numerical trim solver. Moreover, the depth rate increased as the varied volume of the buoyancy control system increased, which suggests that larger volume of the buoyancy control system resulted in greater glide speed.

**FIGURE 10**

Glider motion in the pool. (a) Glider descending. (b) Glider ascending.

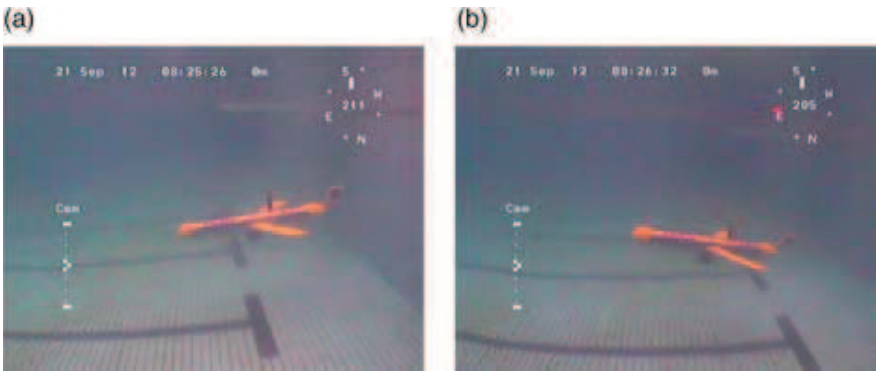


## Conclusions

Glider geometry determines its hydrodynamic characteristics, which further affect the vehicle performance and stability. The geometric parameters are characterized by the slenderness of the hull, the position and shape of the wing, and the size and position of the vertical rudder. The

## FIGURE 11

Glider turning during ascent.

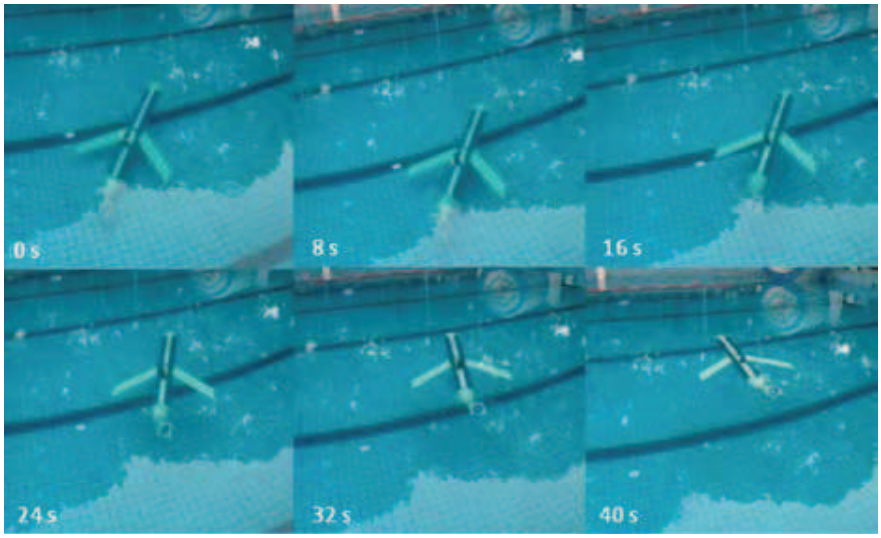


## FIGURE 12

Pitch angle with respect to moving mass displacement.

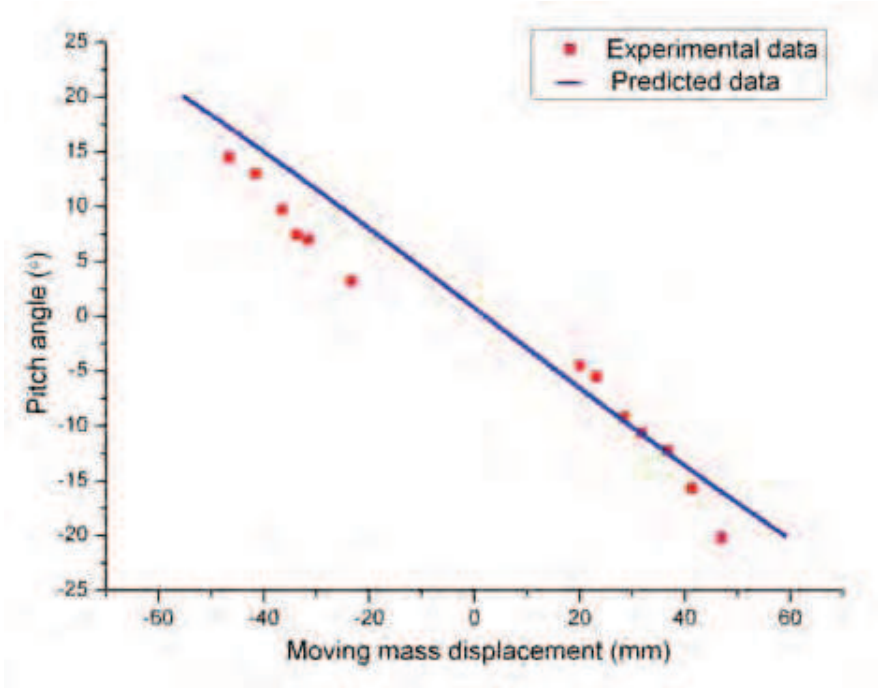


viscous and inviscid coefficients of the *ZJU* glider are obtained by using the computational method and analytical approach, respectively.

A series of theoretical analyses is presented to provide guidelines for vehicle design. Steady flight equilibrium analysis gives the values of operating parameters, such as the varied range of moving mass for pitch control and the varied volume for buoyancy control. We investigate the relationship of glider geometric parameters with the vehicle's performance and stability characteristics. We found, for example, that, for a glider of given mass to maximize the lift-drag ratio at a given minimum glide angle speed, one should increase the hull length, wingspan ratio, and wing aspect ratio and increase or decrease the hull fineness ratio carefully, depending on the required speed. By adapting a regular perturbation approach to develop analytical expressions for steady turning flight, we found that a smaller steering angle is required to effect a steady turn at a given rate when the vertical tail volume is smaller. Turning to stability, we adopt root locus analysis to examine the variation in longitudinal and lateral-directional eigenvalues with changes in wing location and vertical rudder size and location. We determine that the farther aft the wing is located, the more stable the glider longitudinal dynamics become, due in part to the increased pitch damping. The farther aft the vertical rudder is located and the larger the vertical rudder area is, the more stable the glider lateral-directional dynamics become, due to the increasing yaw stiffness and damping. Increased stability may provide better responses to disturbances but may also limit control authority. Considering a tradeoff between stability and control authority, proper design parameters are chosen for our glider development.

Based on the guidelines for vehicle design provided by theoretical analysis, we have completed the development of the *ZJU* glider. A series of tests in a pool have been conducted to evaluate the performance of the glider prototype,

**FIGURE 13**

Depth rate with respect to the varied volume of the buoyancy system.

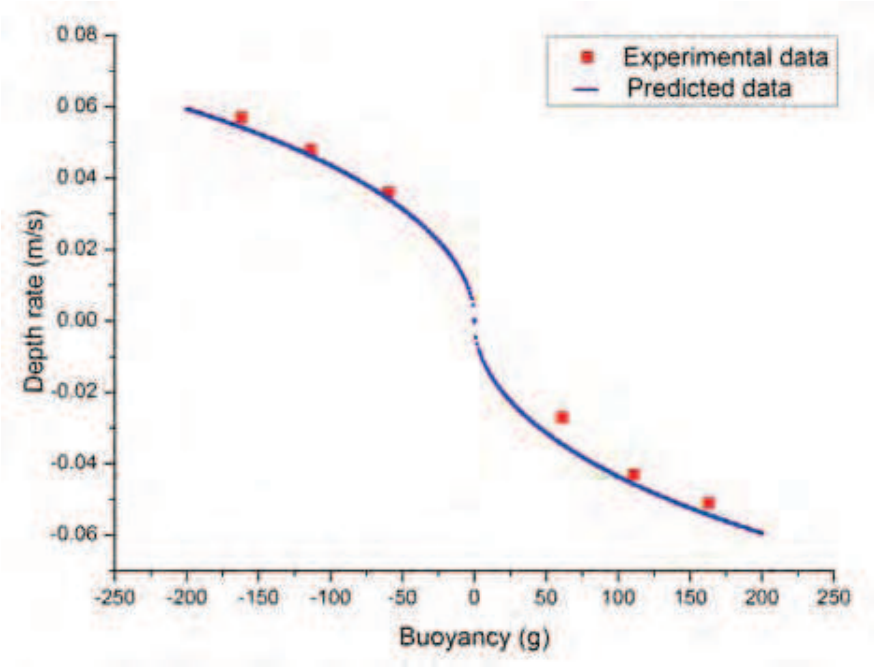


including the sawtooth motion test and the turning motion test. Moreover, a pitch control test has been conducted to investigate the relationship between moving mass displacement and glider pitch angle, and a buoyancy control test has also been conducted to examine the relationship between the varied volume of the buoyancy system and the glide speed. The results not only validate the accuracy of the calculated results of the numerical trim solver but also indicate that the *ZJU* glider is capable of the expected performance of pitch and buoyancy control. Pool trials indicate that *ZJU* glider functions well in water and is capable of serving as a sensor platform for ocean sampling.

Future works include conducting more trials to gain a better understanding of glider operating characteristics and developing effective algorithms for glider motion control and path planning. Moreover, on the basis of the design of the *ZJU* glider, we are developing a hybrid glider for underwater docking (Peng et al., 2013). If the docking station is connected to a cabled ocean observatory (Chen et al., 2012a, 2012b, 2013), the hybrid gliders can be considered as additional mobile nodes for three-dimensional ocean observation. For future application, a fleet of such gliders and hybrid gliders would be used to perform adaptive ocean sampling in the East China Sea, as proposed by Leonard et al. (2010), Fiorelli et al. (2006), and Paley et al. (2008).

## Acknowledgments

This study was supported by the Science Fund for Creative Research Groups of National Natural Science Foundation of China (No. 51221004) and the Program for Zhejiang Leading Team of S&T Innovation (Grant No. 2010R50036).

The authors gratefully acknowledge Professor Craig A. Woolsey for sharing his insights concerning the performance and stability analysis of underwater gliders. The authors also appreciate the helpful feedback from the anonymous reviewers.

## Corresponding Author:

Shilin Peng
The State Key Lab of Fluid Power Transmission and Control
Zhejiang University, Hangzhou 310027, China
Email: pengshilin@zju.edu.cn

## References

**Bhatta**, P. 2006. Nonlinear stability and control of gliding vehicles. Ph.D. thesis, Princeton University, 221 pp.

**Chen**, Y., Yang, C., Li, D., Jin, B., & Chen, Y. 2012a. Design and application of a junction box for cabled ocean observatories system. Mar Technol Soc J. 46(3):50-63. http://dx.doi.org/10.4031/MTSJ.46.3.4.

**Chen**, Y., Yang, C., Li, D., Jin, B., & Chen, Y. 2012b. Study of a DC power system for a multi-node cabled ocean observatories system. J Zhejiang Univ-Sc C. 13(8):613-23. http://dx.doi.org/10.1631/jzus.C1100381.

**Chen**, Y., Yang, C., Li, D., Jin, B., & Chen, Y. 2013. Study on 10kVDC powered junction box for cabled ocean observatory system. China Ocean Eng. 27(2):265-75. http://dx.doi.org/10.1007/s13344-013-0023-y.

**Eriksen**, C.C., Osse, T.J., Light, R.D., Wen, T., Lehman, T.W., Sabin, P.L., … Chiodi, A.M. 2001. Seaglider: A long-range autonomous underwater vehicle for oceanographic research. J Ocean Eng. 26(4):424-36. http://dx.doi.org/10.1109/48.972073.

**Etkin**, B., & Reid, L.D. 1996. Dynamics of flight: Stability and control. New York, NY: John Wiley and Sons. 400 pp.

**Fan**, S.S., & Woolsey, C.A. 2013. Elements of underwater glider performance and

stability. Mar Technol Soc J. 47(3):81-98. http://dx.doi.org/10.4031/MTSJ.47.3.4.

**Fan**, S.S., Yang, C.J., Peng, S.L., Li, K.H., Xie, Y., & Zhang, S.Y. 2013. Underwater glider design based on dynamic model analysis and prototype development. J Zhejiang Univ-Sc C. 14(8):583-99.

**Fiorelli**, E., Leonard, N.E., Bhatta, P., Paley, D.A., Bachmayer, R., & Fratantoni, D.M. 2006. Multi-AUV control and adaptive sampling in Monterey Bay. IEEE J Oceanic Eng. 31(4):935-48. http://dx.doi.org/10.1109/JOE.2006.880429.

**Fossen**, T.I. 1995. Guidance and Control of Ocean Vehicles. New York, NY: John Wiley and Sons, Inc. 162 pp.

**Geisbert**, J.S. 2007. Hydrodynamic modeling for autonomous underwater vehicle using computational and semi-empirical methods. Master thesis, Virginia Tech. 87 pp.

**Graver**, J.G. 2005. Underwater gliders: Dynamics, control and design. Ph.D. thesis, Princeton University. 273 pp.

**Hoerner**, S.F. 1965. Fluid Dynamic Drag. Midland Park, NJ: Author. 452 pp.

**Hussain**, N.A.A., Arshad, M.R., & Mohd-Mokhtar, R. 2011. Underwater glider modelling and analysis for net buoyancy, depth and pitch angle control. Ocean Eng. 36(8):1782-91.

**Jenkins**, S.A., Humphreys, D.E., Sherman, J., Osse, J., Jones, C., Leonard, N.E., … Wasyl, J. 2003. Underwater glider system study. Technical report No. 53, Scripps Institution of Oceanography, University of California, San Diego, CA.

**Leonard**, N.E., & Graver, J.G. 2001. Model-based feedback control of autonomous underwater gliders. IEEE J Oceanic Eng. 26(4):633-45. http://dx.doi.org/10.1109/48.972106.

**Leonard**, N.E., Paley, D.A., Davis, R.E., Fratantoni, D.M., Lekien, F., & Zhang, F. 2010. Coordinated control of an underwater glider fleet in an adaptive ocean sampling field experiment in Monterey Bay. J Field Robot. 27(6):718-40. http://dx.doi.org/10.1002/rob.20366.

**Lewandowski**, E.M. 2004. The Dynamics of Marine Craft: Maneuvering and Seakeeping. River Edge, NJ: World Scientific Pub. Co. Inc. 300 pp.

**Mahmoudian**, N. 2009. Efficient motion planning and control for underwater gliders. Ph.D. thesis, Virginia Polytechnic Institute and State University. 110 pp.

**Mahmoudian**, N., & Woolsey, C. 2008. Underwater glider motion control. In: 47th IEEE Conference on Decision and Control, pp. 552-7. Cancun, Mexico: IEEE.

**Mahmoudian**, N., Geisbert, J., & Woolsey, C. 2010. Approximate analytical turning conditions for underwater gliders: Implications for motion control and path planning. IEEE J Oceanic Eng. 35(1):131-43. http://dx.doi.org/10.1109/JOE.2009.2039655.

**Nelson**, R.C. 1989. Flight Stability and Automatic Control. New York, NY: McGraw-Hill. 284 pp.

**Paley**, D.A., Zhang, F.M., & Leonard, N.E. 2008. Cooperative control for ocean sampling: The glider coordinated control system. IEEE T Contr Syst T. 16(4):735-44. http://dx.doi.org/10.1109/TCST.2007.912238.

**Pamadi**, B.N. 2004. Performance, Stability, Dynamics and Control of Airplanes. Reston, VA: AIAA. 780 pp. http://dx.doi.org/10.2514/4.862274.

**Peng**, S., Yang, C., Fan, S., Zhang, S., Wang, P., Xie, Y., & Chen, Y. 2013. A hybrid underwater glider for underwater docking. In: MTS/IEEE Oceans. San Diego, CA: Marine Technology Society. pp. 1-7.

**Rudnick**, D.L., Davis, R.E., Eriksen, C.C., Fratantoni, D.M., & Perry, M.J. 2004. Underwater glider for ocean research. Mar Technol Soc J. 38(1):48-59.

**Schmidt**, L.V. 1998. An Introduction to Aircraft Flight Dynamics. Reston, VA: AIAA. 397 pp. http://dx.doi.org/10.2514/4.862052.

**Sherman**, J., Davis, R.E., & Owens, W.B., Valdes, J. 2001. The autonomous underwater glider "Spray". IEEE J Oceanic Eng. 26(4):437-46. http://dx.doi.org/10.1109/48.972076.

**Stengel**, R.F. 2004. Flight Dynamics. Princeton, New Jersey: Princeton University Press. 845 pp.

**Stommel**, H. 1989. The slocum mission. Oceanography. 2(1):22-5. http://dx.doi.org/10.5670/oceanog.1989.26.

**Wang**, S., Sun, X., Wang, Y., Wu, J., & Wang, X. 2011. Dynamic modeling and motion simulation for a winged hybrid-driven underwater glider. China Ocean Eng. 25(1):97-112. http://dx.doi.org/10.1007/s13344-011-0008-7.

**Wang**, Y., & Wang, S. 2009. Dynamic modeling and three-dimensional motion analysis of underwater gliders. China Ocean Eng. 23(3):489-504.

**Webb**, D.C., Simonetti, P.J., & Jones, C.P. 2001. SLOCUM: An underwater glider propelled by environmental energy. IEEE J Oceanic Eng. 26(4):447-52. http://dx.doi.org/10.1109/48.972077.

**Yu**, J.C., Zhang, A.Q., Jin, W.M., Chen, Q., Tian, Y., & Liu, C.J. 2011. Development and experiments of the Sea-Wing underwater glider. China Ocean Eng. 25(4):721-36. http://dx.doi.org/10.1007/s13344-011-0058-x.

**Yu**, J.C., Zhang, F.M., Zhang, A.Q., Jin, W.M., & Tian, Y. 2013. Motion parameter optimization and sensor scheduling for the Sea-Wing underwater glider. IEEE J Oceanic Eng. 38(2):243-54. http://dx.doi.org/10.1109/JOE.2012.2227551.

**Zhang**, S.W., Yu, J.C., Zhang, A.Q., & Zhang, F.M. 2013. Spiraling motion of underwater gliders: Modeling, analysis, and experimental results. Ocean Eng. 60:1-13. http://dx.doi.org/10.1016/j.oceaneng.2012.12.023.